Applied Catalysis B: Environmental 245 (2019) 130–142

Contents lists available at ScienceDirect

Applied Catalysis B: Environmental

journal homepage: www.elsevier.com/locate/apcatb

In-situ Fe-doped g-C_3N_4 heterogeneous catalyst via photocatalysis-Fenton reaction with enriched photocatalytic performance for removal of complex wastewater

Jinshan Hu, Pengfei Zhang, Weijia An, Li Liu, Yinghua Liang*, Wenquan Cui*

College of Chemical Engineering, Hebei Key Laboratory for Environment Photocatalytic and Electrocatalytic Materials, North China University of Science and Technology, Tangshan 063210, PR China

ARTICLE INFO

Keywords:
Fe-g-C_3N_4
Photocatalysis-Fenton system
Phenol
Complex wastewater
H_2O_2

ABSTRACT

In this work, an in-situ Fe-doped g-C_3N_4 catalyst was synthesized by thermal shrinkage polymerization. A heterogeneous photocatalysis-Fenton system was formed with the addition of H_2O_2 under visible irradiation and exhibited excellent and recyclable removal performance for refractory contaminants such as: phenol, bisphenol A, 2, 4-dichlorophenol and coking wastewater, which was due to the formation of σ-π bonds via Fe and N element in the triazine ring skeleton of Fe-g-C_3N_4. The electrons generated can be quickly transferred to Fe^{3+} to form Fe^{2+} under the interaction of the chemical bond. The efficiency of photoelectron separation was accelerated, and ˙OH radicals were quickly generated with the reaction between Fe^{2+} and H_2O_2. Specifically, the recycling of Fe can be achieved in the heterogeneous system, which avoids the problems for the recycling and secondary pollution of Fe ions in homogeneous Fenton reaction. Parameters such as Fe doping amount, hydrogen peroxide concentration, pH value, catalyst concentration, and complex wastewater (coking wastewater) were optimized. The degradation of coking wastewater were also performed, and the chemical oxygen demand (COD) and total organic carbon (TOC) values for 300 ml coking wastewater could be reduced from 64.6 and 25.3 mg/L to 22.8 and 12.3 mg/L in 60 min, respectively. These results demonstrate photocatalysis-Fenton reaction with Fe-g-C_3N_4 catalyst is promising for environmental remediation.

1. Introduction

Environmental pollution and energy shortages are important global problems. Water pollution from organic molecules is particularly troubling [1–4]. Organic pollutants include organic phenols, polycyclic aromatic hydrocarbons and other harmful substances [5]. Once entering the water, it is difficult to biodegrade and long-term accumulation can cause serious harm to humans [6]. Organic pollutants are currently removed by adsorption, electrochemical oxidation, photocatalytic oxidation, ozone oxidation and Fenton oxidation [7–12]. Fenton oxidation offers strong adaptability to pollutants and low energy consumption. It is one of the most mature methods for advanced treatment of organic pollutants in water. The Fenton oxidation process includes Fe^{2+} and H_2O_2 to produce Fe^{3+} and ˙OH [13]. The ˙OH can mineralize organic pollutants especially refractory phenols. However, the recovery of Fe^{2+} is extremely slow [11]. Thus, the removal of organic pollutants in the Fenton reaction is restricted and often requires the addition of excessive H_2O_2, which makes the Fenton method expensive. In addition, the existing Fenton method is a homogeneous reaction system with adding an iron salt to the water. The reaction makes it difficult to separate the catalyst from the reaction system. This can cause pollution from the Fe ion as well as a loss of catalyst.

Photocatalysis uses light energy without other energy sources and no secondary pollution. Therefore, it has utility in solving environmental pollution. Sunlight can excite semiconductors to make photoelectron-hole pairs and generate active radicals (˙OH, $˙O^{2-}$); these active radicals can destroy or mineralize organic pollutants [14–16]. Current photocatalysis materials include inorganic semiconductor materials such as TiO_2 and ZnO [17,18]. Recently, many photocatalytic materials have been modified. For example, Zhu et al. [19] used g-C_3N_4 and TiO_2 form a core/shell structure composite catalyst that improved the visible light utilization efficiency and the degradation activity. Sakthivel et al. [20] used the rapid transfer of graphdiyne to form graphdiyne-ZnO nanohybrids with a one-fold increase in the rate constant for degradation of ZnO monomers. Although the activity of catalytic degradation is improved, there are still bottlenecks such as low

* Corresponding authors.
E-mail addresses: liangyh@ncst.edu.cn (Y. Liang), wqcui@ncst.edu.cn (W. Cui).

https://doi.org/10.1016/j.apcatb.2018.12.029
Received 6 September 2018; Received in revised form 17 November 2018; Accepted 10 December 2018
Available online 11 December 2018
0926-3373/

utilization of visible light and low separation efficiency of photoelectrons and holes. This restricts the popularization and application of photocatalytic methods in the advanced treatment of organic pollutants.

The photocatalysis-Fenton system consists of both photocatalysis and Fenton reactions. It shows excellent ability to remove organic pollutants. Electrons promote the decomposition of H_2O_2 to generate $^{\cdot}OH$ and the remaining holes are further oxidized to generate $^{\cdot}OH$ [21–23]. This can further promote the removal of organic pollutants. Cai et al. [24] used $ZnFe_2O_4$ as a catalyst and added H_2O_2 and Fe to form a Fenton reaction that degrades Orange II. This showed excellent removal ability. Sun et al. [25] loaded Fe_3O_4 to TiO_2 and added hydrogen peroxide. The apparent kinetic constant of the reaction that catalyzed by Fe_3O_4-TiO_2 was about 5.3 and 8.3 times of that catalyzed by TiO_2 or Fe_3O_4. These results proved that synergistic operation of photocatalytic degradation and Fenton process. However, this research focuses mainly on a single pollutant. There are few reports on the degradation behavior of complex organic wastewaters. The mechanism of the photocatalysis-Fenton system process remains unclear and the influence of reaction parameters on activity has not yet been systematically studied.

The graphite-like carbon and nitrogen compound (g-C_3N_4) is a nonmetallic semiconductor that consists only of C and N. Its band gap is about 2.7 eV and it absorbs visible light. It is also resistant to acids, alkalis and light corrosion. It has good stability and its structure and properties are easily regulated. It has good photocatalytic properties and is a research hotspot in the field of photocatalytic [26–29]. Elemental doping can further regulate the band gap structure of g-C_3N_4. This promotes the separation of light-generated electrons and holes. Wang et al. [30] found that F doping in the CN matrix forms a C-—F bond that can increase the absorption range of light. Hu and Song et al. [31,32] also conducted an on Fe-doped g-C_3N_4, and observed enhanced adsorption of light in the 450–700 nm regions, which led to improved photocatalytic degradation of RhB (Rhodamine B) under visible light irradiation. Ma et al. [33] loaded Fe onto g-C_3N_4 and promoted the Fenton-like reaction by using π-π structure. This indicates that g-C_3N_4 shows good catalytic performance in the field of environmental remediation.

Here, Fe-g-C_3N_4 was synthesized which explore the efficiency of complex wastewater removal under a heterogeneous photocatalysis-Fenton system. This overcomes the problems of slow H_2O_2 catalytic decomposition and pollution from Fe ions dissolved in water in the homogeneous Fenton reaction system. It also promotes the separation of photoelectrons and holes. The mechanism of photocatalysis-Fenton system was explored and the reaction conditions were optimized through the degree of phenol removal. The product offered efficient removal of organic matter in complex wastewater.

2. Experimental

2.1. Synthesis of Fe-g-C_3N_4

In a typical procedure, 5 g of dicyandiamide was dissolved in 20 mL deionized water at 80 °C and then $FeCl_3$ was added to this solution and stirred for 1 h. The mixture was continually stirred at 120 °C until the water was completely evaporated. The dried mixture was then ground and heated to 550 °C in a nitrogen atmosphere at 2 °C/min and held there for 4 h. The resulting product was denoted as Fe-g-C_3N_4 (Scheme 1). We used different mass ratios of $FeCl_3$ and dicyandiamide: 1%, 3%, 5%, 7% and 9% Fe-g-C_3N_4. The g-C_3N_4 was prepared without adding $FeCl_3$ under the same conditions.

For comparison, a mechanically mixed sample of g-C_3N_4 with $FeCl_3$ was prepared, and the sample is denoted as M-Fe-g-C_3N_4. (The content of Fe in mechanically mixed sample g-C_3N_4 and Fe content in 5% Fe-g-C_3N_4 are both 4.2%).

2.2. Characterization of materials

The crystal structure was probed by X-ray diffraction (XRD) using a D MA X 2500 pc Rigaku diffractometer (CuK_α radiation, operating voltage = 40 kV, operating current = 100 mA, current density = 100 mA, scanning range = 5–80°). The morphology and size of catalyst particles were characterized by field emission scanning electron microscopy (FE-SEM; S-4800, Hitachi, Japan) and transmission electron microscopy (TEM; JEOL JEM-2010). UV–vis diffuse reflectance spectroscopy (Puxi, UV1901) was used for optical absorption measurements. Fourier transform infrared (FTIR) spectra were recorded on an IR Vertex 70 FTIR spectrometer. X-ray photoelectron spectroscopy (XPS) measurements were carried out using an XSAM800 apparatus. The ZATA potential of the catalyst was recorded on ZETA potential and nanoparticle size analyzer (Zetasizer Mano zs9003030810). Phenol removal intermediates were detected using LCMS (PR-LCMS-2020). A simultaneous quantitative analysis of C and N was performed with the Vario EL III (Elementar Analysensysteme GmbH, Germany) elemental analyzer. The electrochemical performance of samples was characterized using a three-electrode quartz cell and a CHI660E electrochemical workstation in 0.1 M Na_2SO_4 electrolyte using Pt foil used as a counter electrode and a saturated calomel electrode as the reference. The photoluminescence (PL) spectra were recorded on a Hitachi F-7000 spectrometer; the excitation wavelength is 315 nm. The concentration of Fe in the catalyst and Fe ion leaching rates in organic pollutants was detected by an atomic absorption spectrophotometer (Puxi TAS-990).

2.3. Organic pollutant removal and catalytic mechanism

Removal of organic pollutants by the photocatalysis-Fenton system was tested in a photocatalytic multi-test tube light reaction instrument (Nanjing Xujiang Machine Power Plant XPA-7). The light reaction instrument was connected to a cooling device to keep the reaction solution temperature constant at 25 ± 2 °C. We used a 350 W xenon lamp (ultraviolet light was filtered at wavelengths < 420 nm) as a visible light source for vertical irradiation. Catalyst was used to degrade 50 mL of organic pollutants. The reaction solution was stirred for 30 min in the dark. Then, H_2O_2 was added and the lamp was turned on for catalytic reaction. A 1 mL sample of the reaction suspension was studied every 10 min. The obtained sample was filtered and phenol concentration was detected by high performance liquid chromatography (HPLC). In the comparison experiments, the amount of Fe_2O_3 added was calculated to ensure that the content of Fe in Fe_2O_3 is consistent with the content of Fe in Fe-g-C_3N_4.

In the coking wastewater removal experiment, 300 ml of coking wastewater (COD 64.6 mg/L and TOC 25.3 mg/L) was placed in a 500 ml beaker along with catalyst and H_2O_2 with a 500-W xenon lamp as a light source. The rotation speed was held at 400 r/min. Aliquots were removed periodically for study and the degree of removal was expressed in terms of changes the organic pollutants concentration (OPC), COD and TOC, respectively. The removal efficiency formula is defined as:

$$\text{Removal efficiency}(\%) = \frac{C_0 - C}{C_0} \times 100 \quad (1)$$

The OPC values of phenol, bisphenol A and 2, 4-dichlorophenol were detected by HPLC. One ml of the reaction solution was filtered through a 2 μm membrane to remove the catalyst; methanol/water (70/30, v/v) was the mobile phase with an elution time of 10 min and a detector wavelength of 280 nm A C18 reverse-phase column (Agilent 1100, 4.6 nm × 200 nm) was used for chromatographic analysis. The changes in solution concentration were studied before and after the reaction.

The TOC was measured using a total organic carbon analyzer (Shimadzu Corporation TOC-L CPH, Japan). A 15 ml sample was centrifuged to remove the catalyst. The NPOC method was used for

Scheme 1. Scheme for the fabrication of Fe-g-C_3N_4.

detection.

The COD was measured via titration with potassium dichromate. The sample was centrifuged to remove the catalyst and then 10 ml was removed and placed in an Erlenmeyer flask. Next, 5 ml of 0.25 M potassium dichromate and 15 mL of sulfuric acid were added. This was refluxed for 2 h and then cooled after adding 45 ml distilled water to rinse the condenser tube. Then added three drops of ferrioxide indicator and titrated it with 0.05 M ferrous ammonium sulfate solution. The color changed from yellow to blue-green and finally to red brown. This is the endpoint of the titration; the COD was calculated according to the formula. (Each experiment had a blank that used 10 ml distilled water instead of water sample with other steps remaining the same.)

$$\rho = \frac{C \times (V_0 - V_1) \times 8000}{V_2} \quad (2)$$

In the formula:

C: Ammonium ferrous sulfate standard solution concentration, M

V_0: Blank sample consumption volume of ammonium ferrous sulfate standard solution, ml

V_1: Determination of the volume of ammonium ferrous sulfate standard solution consumed in water samples, ml

V_2: Sample volume, ml

Trapping experiments explored the generation of active species via the photocatalysis-Fenton system and their impact on phenol removal efficiency. The trapping agents for the experiment were isopropyl alcohol (˙OH), p-benzoquinone ($\dot{O}^{2-}$), EDTA-2Na (h^+) and Cr (VI) (e^-) [24,34,35]. The trapping experiments were the same as the organic pollutants removal experiment with isopropyl alcohol; p-benzoquinone, EDTA-2Na; potassium dichromate were added to a 50 ml phenol solution, respectively. The trapping agent's concentration was 5 mM. The reaction was activated in the photochemical reaction apparatus and 1 ml of the sample was removed at 10 min; the phenol removal efficiency was evaluated by HPLC.

Detection of hydroxyl radicals used p-phthalic acid and ˙OH reaction to generate high-fluorescence substances, that were detected with a fluorescence spectrophotometer (Hitachi F-7000FL) according to the intensity of the generated fluorescence peak to determine the concentration of generated ˙OH. We then tested 50 ml of 5×10^{-4} M phthalic acid instead of 20 ppm phenol solution in the photochemical reaction apparatus for reaction. Again, aliquots were removed every 20 min. These were centrifuged to remove the catalyst. Product was detected with a fluorescence spectrophotometer at an excitation wavelength of 332 nm [36,37].

3. Results and discussion

3.1. The photocatalysis-Fenton system improves phenol removal ability and structure characterization of catalyst

The phenol degradation removal results for photocatalysis, heterogeneous Fenton reaction and photocatalysis-Fenton reaction are shown in Fig.1a. The phenol could neither be degraded by H_2O_2 in the dark nor under irradiation indicating that H_2O_2 does not produce ˙OH without catalyst [25]. The efficiency of phenol removal in the heterogeneous Fenton reaction with Fe-g-C_3N_4 and Fe_2O_3 was 90.0% and 5.3% in 50 min and the removal efficiency in the photocatalysis-Fenton system with Fe-g-C_3N_4 and M-Fe-g-C_3N_4 was 100.0% and 96.2% in 50 min. This result indicated that Fe in catalyst with H_2O_2 forms a heterogeneous Fenton reaction and converts H_2O_2 to ˙OH and increases phenol removal ability. The removal ability of Fe-g-C_3N_4 is better than that of Fe_2O_3. Under visible light, the photo-generated electrons can accelerate electron transfer from Fe^{3+} to Fe^{2+} with increasing the production of ˙OH. The Fe-g-C_3N_4 removal efficiency is obviously higher than M-Fe-g-C_3N_4 catalysts, which indicated that in situ synthesis of Fe-doped g-C_3N_4 offered faster electron transfer compared to mechanical composite catalysts. Therefore, the photocatalysis-Fenton system promotes the heterogeneous Fenton reactions.

Fig. 1b compares the photocatalysis-Fenton system in terms of photocatalytic removal of phenol. The removal efficiency of g-C_3N_4 and Fe-g-C_3N_4 under visible light irradiation was very low. The addition of H_2O_2 to the g-C_3N_4 reaction system resulted in a removal efficiency of 10.1% by 50 min. After the Fe-g-C_3N_4 was added to H_2O_2, the phenol removal efficiency was 100% at 50 min. This result explained that the valence band position of g-C_3N_4 and Fe-g-C_3N_4 (XPS-VB of g-C_3N_4 and Fe-g-C_3N_4 = 1.40 V) is lower than that of ˙OH ($OH^-/\dot{O}H$ = 1.99 V) [38], difficult to oxidize phenol with highly oxidizing ˙OH. In addition, this experiment uses a high concentration of phenol with a short illumination time. Therefore, the efficiency of removing phenol from g-C_3N_4 and Fe-g-C_3N_4 is very low, which is consistent with other literature reports [19,39,40]. The addition of H_2O_2 to the g-C_3N_4 catalyst reaction system slightly increases the removal efficiency. The photo-generated electrons generated by g-C_3N_4 directly react with H_2O_2 ($H_2O_2 + e^- \rightarrow \dot{O}H + OH^-$) to form ˙OH [41], However low charge transfer efficiency limit the degradation ability. With the presence of H_2O_2, a strong σ-π feedback bond was formed in Fe-g-C_3N_4 due to Fe in situ doping inside the framework of the g-C_3N_4. Thus, the photo-generated charge can be rapidly transferred to Fe^{3+}, so that Fe^{3+} could the reduce to Fe^{2+} and then Fe^{2+} act as the reaction cite to catalyze H_2O_2 to form ˙OH, thus a Fenton reaction had been accelerated via a photocatalysis-Fenton system, recombination of electrons and holes were also inhibited.

The 2D chromatogram of HPLC with photocatalysis-Fenton system removal phenol is shown in Fig. 1c. The retention time of the phenol peak (I) is about 3.3 min. As the reaction time increases, the peak gradually decreases and the peak value at 50 min was zero. Ten minutes after the start of the reaction, a new peak (II) appears in front of the characteristic peak of phenol and peak (II) gradually decreases. This shows that the phenol had been completely degraded after 50 min, and new intermediates were generated [42,43].

SEM and TEM further reveal the morphology and microstructure of the catalyst. Fig. 2a, c and e show g-C_3N_4 images of SEM TEM and HRTEM, respectively. The g-C_3N_4 is a layered massive particle. In Fig. 2b, d and f, 5% Fe-g-C_3N_4 shows a sheet-like structure similar to that of g-C_3N_4. This shows that Fe doping into g-C_3N_4 does not change the sheet structure of g-C_3N_4. Furthermore, iron oxide nanoparticles were not found in the TEM and HRTEM images of 5% Fe-g-C_3N_4 indicating that Fe was ionically doped into the g-C_3N_4 framework. TEM mapping of Fig. 2g illustrates that C, N and Fe elements are evenly

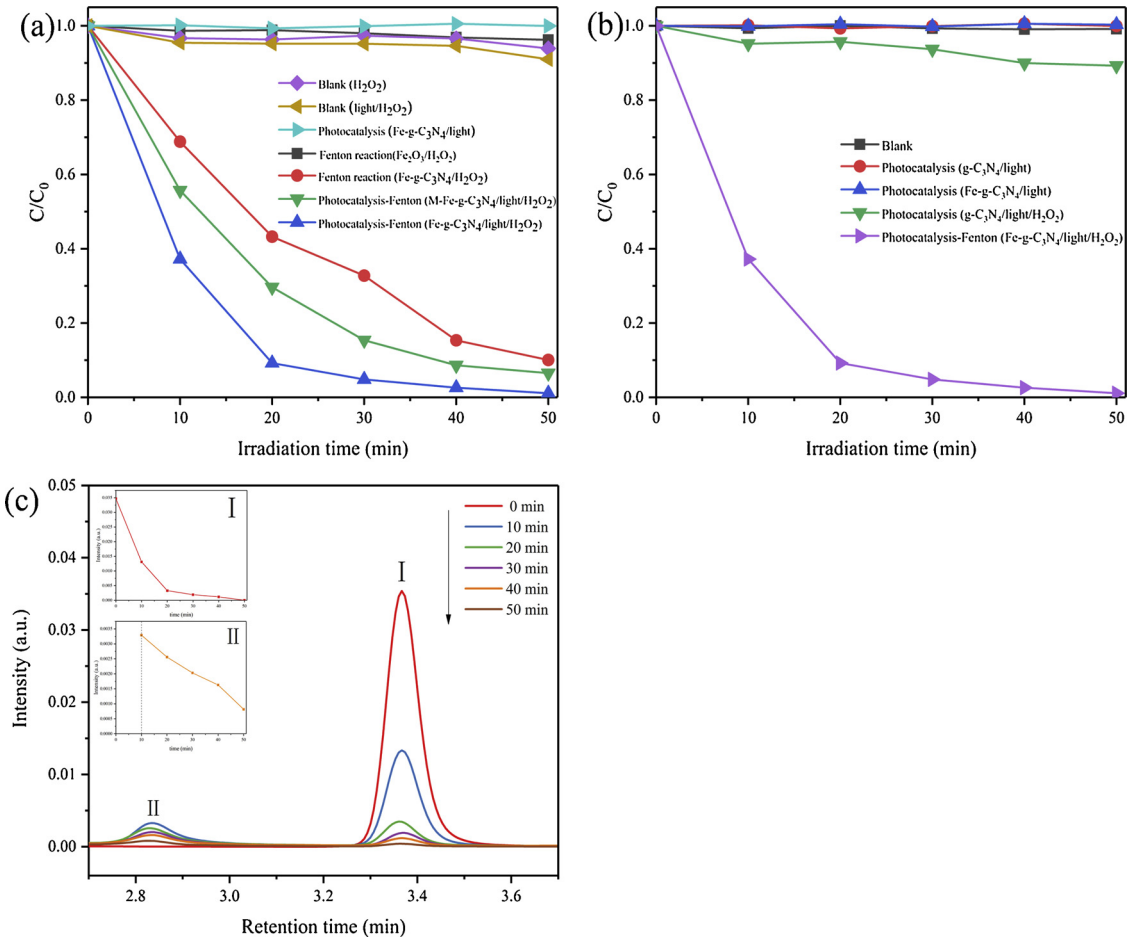

Fig. 1. (a) The photocatalysis-Fenton system promotes the heterogeneous Fenton reaction to remove phenol, (b) Photocatalysis-Fenton system promote photocatalytic to removal efficiency of phenol, (c) Photocatalysis-Fenton system removal of phenol in HPLC 2D chromatograms. (C_0 = 20 ppm, H_2O_2 = 8.0 mM, catalyst = 1.0 g/L, P = 350 W Xenon lamp > 420, T = 25 ± 2 °C).

distributed to the surface of the sheet. TEM-EDS of Fig. 2h shows peaks for Fe, C and N, which further proves that Fe was doped on g-C_3N_4 and the Fe content of 5% Fe-g-C_3N_4 is 4.19% as measured via atomic absorption spectrophotometry. The content of C and N in the catalyst was determined by the elemental analysis, and the content of Fe was determined by an atomic absorption spectrophotometer. The contents of C and N in g-C_3N_4 were 63.12% and 36.37%, respectively. The content of C, N and Fe in Fe-g-C_3N_4 was 60.51%, 34.54%, and 4.19%, respectively.

The chemical states of elements and chemical composition of doping Fe were investigated by XPS. Fig. 3a shows the full spectrum of all the elements of g-C_3N_4 and Fe-g-C_3N_4 catalyst; the peaks of C, N, O were found in the XPS spectra of g-C_3N_4 and the peaks of C, N, O and Fe were found in the XPS spectra of Fe-g-C_3N_4. The Fe peak is very low due to the small amount of Fe doping. Fe was successfully doped into g-C_3N_4 as confirmed by the full spectrum. In Fig. 3b, the XPS C1 s spectrum for g-C_3N_4 can be deconvolved into two peaks with binding energies of 284.63 and 287.79 eV ascribed to sp^2C-C, C—O and ri-s-triazine (heptazine) structures N—C═N bonds [44]. In Fig. 3c, XPS C1 s spectrum for g-C_3N_4 can be deconvolved into three peaks with binding energies of 398.10, 398.94 and 400.23 eV ascribed to the sp^2 structure of N (C═N—C), tertiary N— $(C)_3$ and $-NH_2$ or ═NH energy groups, 404.2 eV ascribed to charge effect [45,46]. In Fig. 3d, the Fe 2p spectrum exhibits two characteristic peaks at 711.11 and 724.35 eV. These are the typical Fe $2p_{3/2}$ and Fe $2p_{1/2}$ signals of Fe^{+3}, respectively [47,48]. In Fig. 3e, the O 1s spectrum exhibits one characteristic peaks at 532.4 eV which was ascribed to surface adsorbed water in the g-C_3N_4 and Fe-g-C_3N_4 [49,50]. The characteristic diffraction peak of Fe-O [51] is not found in the Fe-g-C_3N_4 indicating that Fe was ionically doped into the g-C_3N_4 framework. Versus g-C_3N_4, the peak positions of the C1 s and N1 s in 5% Fe-g-C_3N_4 samples shifted toward the low binding energy and the overall offset of the C1 s shifted lower by 0.07 and 0.19 eV, respectively. The offsets of N1 s orbits are shifted by 1.0, 0.18, 0.43 and 0.41 eV, respectively and the N(C═NC) offset of the sp^2 structure in N1 s is the largest. The XPS results suggest that the sp^2 hybridization orbital of the lone pair of electrons in the tris-triazine ring as well as the d^2sp^3 hybridization of Fe^{3+} forms an σ-π coordination bond (feedback bond). In the tris-s-triazine ring, the sp^2 hybrid orbital of N can be superimposed with the d^2sp^3 hybrid empty orbit of Fe^{3+} and N provides the lone pair electrons to form an σ-bond (Scheme 2a) Furthermore, the Fe^{3+} electron-filled d orbitals and tri-s-triazine ring π orbitals are superimposed and Fe^{3+} provides d electrons into π-bonds (Scheme 2b). The electrons in Fe^{3+} can then be fed back to the σ bond of the tri-S-triazine ring through π coordination to form an σ-π feedback bond. As a result, the outer electron cloud density of C and N elements increases; thus, the atomic repulsive force of the inner electron increases and the binding energy of the C1 s orbit and the N1 s orbit is reduced in the XPS of the Fe-g-C_3N_4 sample. This bonding can achieve d-π conjugate between the d orbital of Fe^{3+} and the large π bond of the tris-S-triazine ring by feedback of the π bond. The electron transfer between g-C_3N_4 and Fe^{3+} could be accelerated by d-π cnjugated large π bond, which rapidly migrates photogenerated electrons to Fe^{3+}. Fe^{3+} is reduced to Fe^{2+} by photogenerated electrons, and then reacts with H_2O_2 to complete the cycle between Fe^{3+} and Fe^{2+}, achieving the synergy between photocatalysis and Fenton reaction, improving the photocatalytic activity and achieving the purpose of efficiently degrading pollutants.

Fig. 4a shows the XRD patterns of g-C_3N_4 and Fe-g-C_3N_4. All

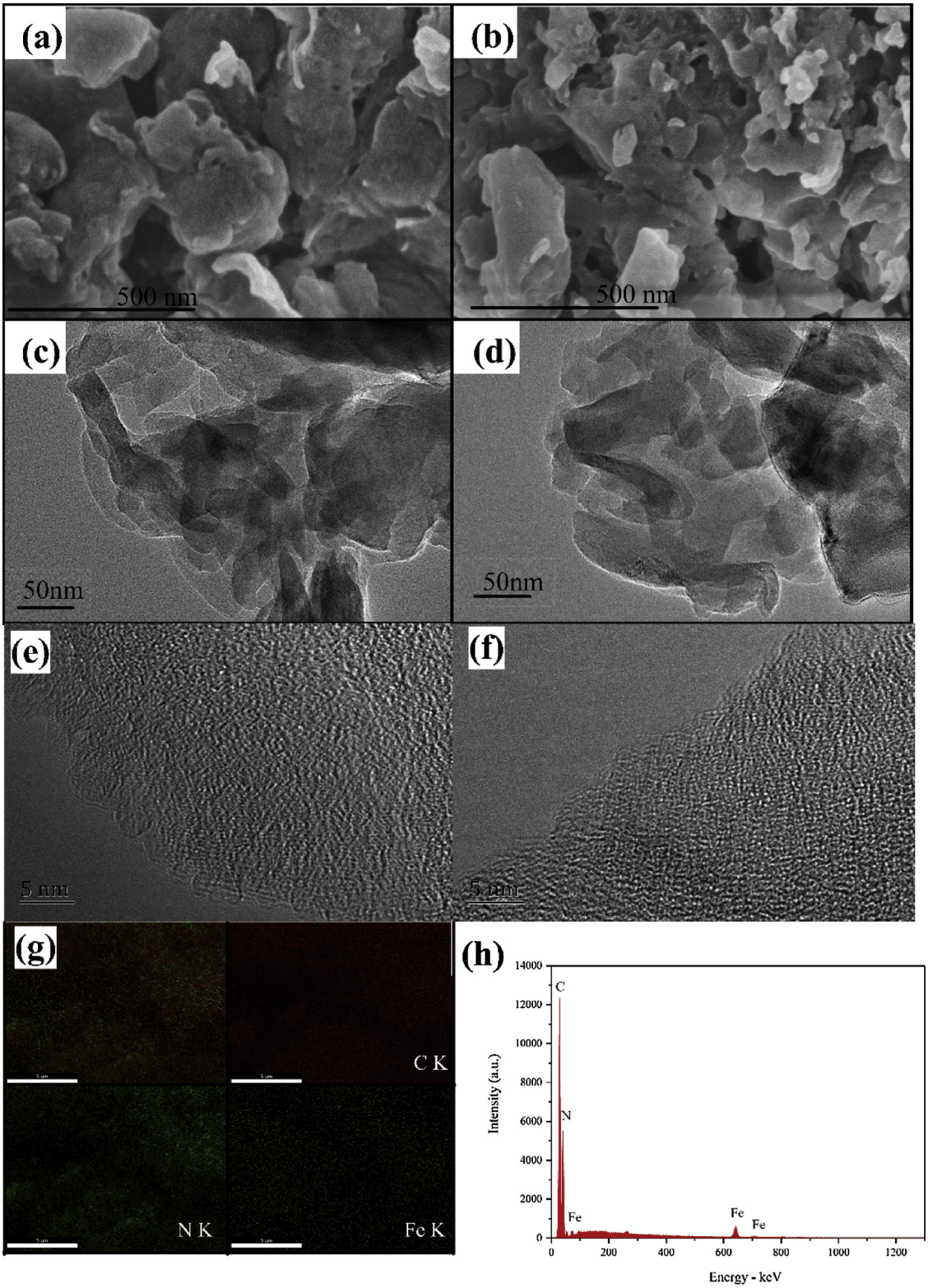

Fig. 2. (a) SEM images of g-C_3N_4, (b) SEM images of 5% Fe-g-C_3N_4, (c) TEM images of g-C_3N_4, (d) TEM images of 5% Fe-g-C_3N_4, (e) HRTEM images of g-C_3N_4, (f) HRTEM images of 5% Fe-g-C_3N_4, (g)TEM mapping of 5% Fe-g-C_3N_4, (h) TEM EDS image of 5% Fe-g-C_3N_4.

catalysts have diffraction peaks at 13.1° and 27.4°, which are consistent with the standard card (JCPDS 87–1526). The peaks are (100) and (002) diffraction peaks [52]. As the Fe content in g-C_3N_4 increases, the intensity of the diffraction peaks of the (100) and (002) planes gradually weakened. The crystallinity of the (100) and (002) crystal planes decreases because Fe affects the thermal condensation of dicyandiamide. Comparison of XRD between Fe-g-C_3N_4 and Fe_2O_3, the diffraction peak of Fe oxide was not found in Fe-g-C_3N_4. Fig. 4b shows the FT-IR spectra of g-C_3N_4 and Fe-g-C_3N_4. We note that g-C_3N_4 at 1640 cm^{-1} and 1240 cm^{-1} (I) correspond to the stretching vibration of C═N and CN bonds [53]. The normal vibration of the triazine structure corresponds to the peak at the 808 cm^{-1} (II) position. The 3180 cm^{-1}

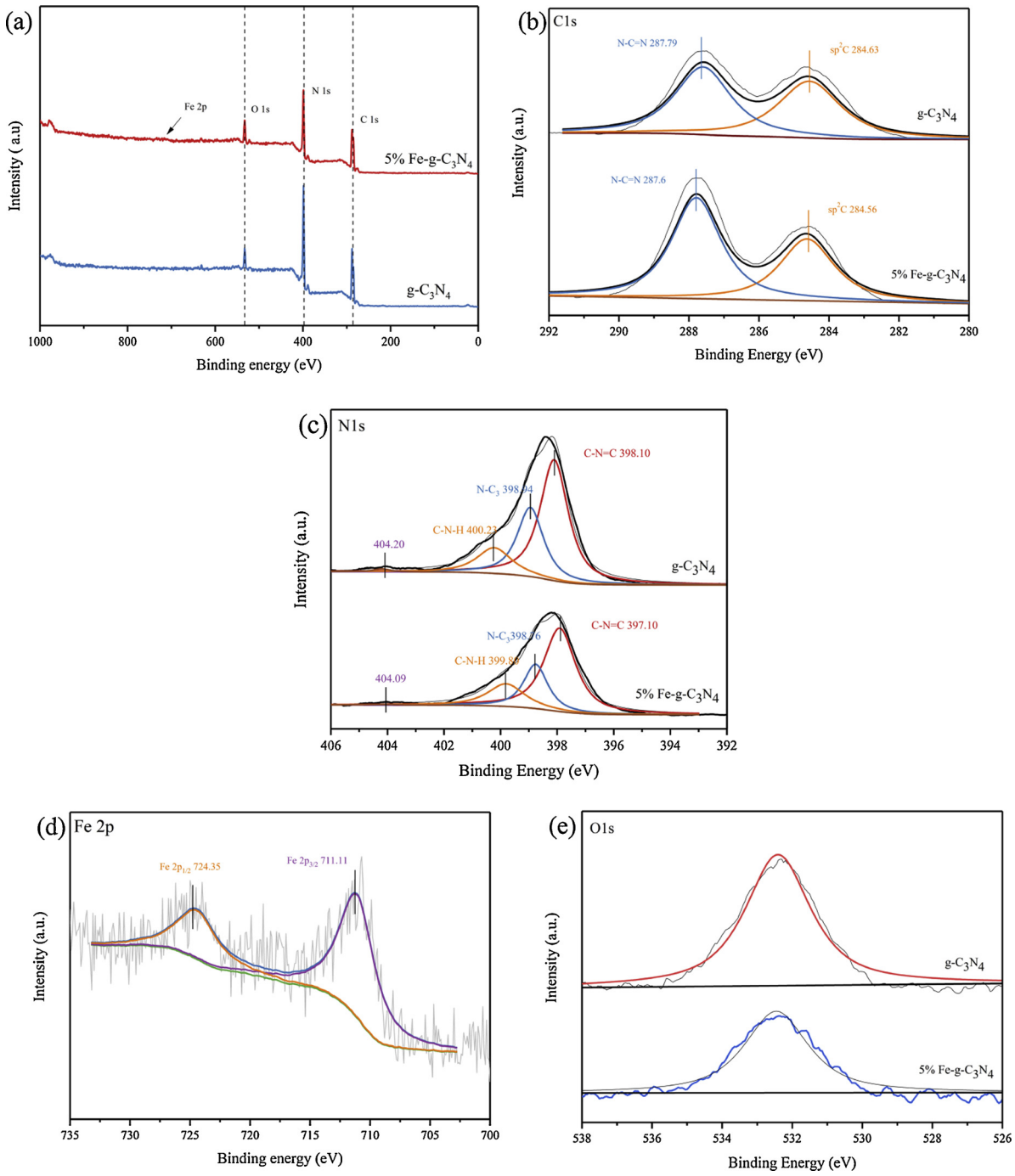

Fig. 3. The XPS spectra of whole XPS spectra (a) and typical elements C 1 s (b), N 1 s (c), Fe 2p (d), O 1 s (e).

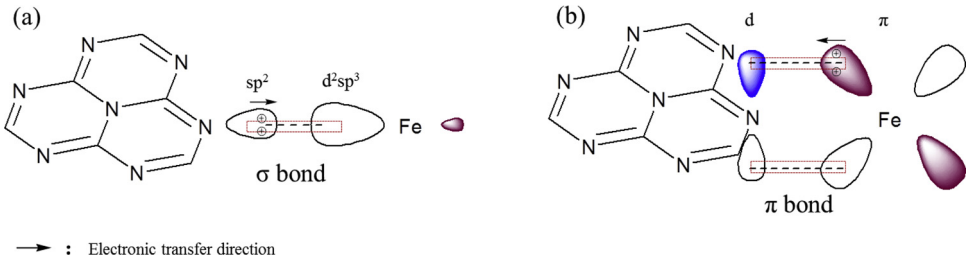

Scheme 2. Scheme for forming σ-π bond of Fe-g-C_3N_4.

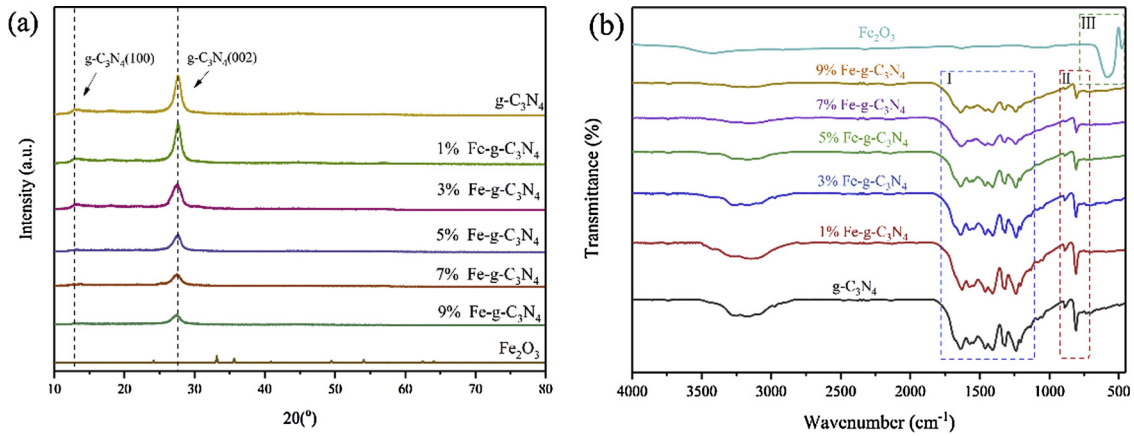

Fig. 4. (a) XRD patterns of Fe_2O_3, g-C_3N_4 and Fe-g-C_3N_4, (b) FTIR spectra of Fe_2O_3, g-C_3N_4 and Fe-g-C_3N_4.

peak corresponds to the N—H stretching vibration [54], which indicates that amino groups are still present in g-C_3N_4 formed by polycondensation of dicyandiamide. The peaks did not shift with different amounts of Fe doping into g-C_3N_4, but the corresponding peaks did gradually weaken. This shows that Fe does not change the skeletal structure of g-C_3N_4. The peaks appears at 556 and 471 cm^{-1} (III) in Fe_2O_3 as shown in Fig. 4b were the characteristic stretching vibrations of the Fe-O bond in hematite particles [55]. These peaks were not detected in Fe-g-C_3N_4. This further confirms that Fe was ion-doped into the g-C_3N_4 skeleton similar to the TEM and XPS results.

Fig. 5a shows the UV–vis diffuse reflectance spectra of g-C_3N_4 and Fe-g-C_3N_4. The g-C_3N_4 and Fe-g-C_3N_4 shows strong light absorption from UV to visible light. The absorption range of Fe-g-C_3N_4 complex is red-shifted compared to g-C_3N_4. This suggests that the catalyst can improve the effective utilization of solar energy and enhance the catalytic activity of visible light. Fig. 5b shows the Kubelka-Munk function curve of g-C_3N_4 and Fe-g-C_3N_4. The transition bandgaps estimated from the onset of the curve edges were about 2.72 and 2.50 eV for g-C_3N_4 and Fe-g-C_3N_4. The relatively narrow band gap energy observed for Fe-g-C_3N_4 may be attributed to the feedback build-up between Fe and N, which enables more efficient use of the solar spectrum.

3.2. Photocatalysis-Fenton system mechanism of Fe-g-C_3N_4

The separation effect of electron-hole pairs can be proved by the electrochemical properties of the catalyst. Fig. 6a shows that the photocurrent response of Fe-g-C_3N_4 is 1.8 times higher that of g-C_3N_4 under the same conditions. Photoelectrons generated by g-C_3N_4 can be quickly transferred to Fe under the action of the σ-π feedback bonds. Therefore, the separation of photo-generated electron hole pairs is promoted. Fig. 6b compares the photocurrent of the catalyst after adding H_2O_2 in the reaction system. When H_2O_2 was added to the reaction system, the photocurrent intensity was reduced by 63% indicating that the photo-generated electrons were not transmitted to the counter electrode through the external circuit during testing. Electrons participate in the Fenton reaction and promote the formation of Fe^{2+}.

Fig. 6c shows EIS plots of g-C_3N_4, Fe-g-C_3N_4 and Fe-g-C_3N_4 before and after H_2O_2 addition with 500 W xenon lamps (> 420 nm). The EIS showed that the radius of Nynquist curve of Fe-g-C_3N_4 catalyst is lower than that of g-C_3N_4 further illustrating that Fe doping accelerates the carrier transport on the surface of the catalyst and facilitates the separation of photo-generated electrons and holes. In the Fe-g-C_3N_4 catalyst, the Nyquist curve slightly increased in the H_2O_2 system. This is due to the formation of Fenton reaction after the addition of H_2O_2, which promotes the formation of Fe^{2+} and consumes photo-generated electrons.

The charge separation efficiency was further tested by PL measurements. Fig. 6d shows that g-C_3N_4 produces a high-intensity fluorescence peak at 440 nm and Fe-g-C_3N_4 has a 74% decrease in fluorescence intensity compared to g-C_3N_4 indicating that electrons and holes generated by g-C_3N_4 have a very high recombination rate; Fe doping to g-C_3N_4 can effectively inhibit the recombination of photo-generated electrons and holes. Photoelectrons can be transferred to Fe by chemical bonding and this reduces the recombination efficiency of the photoelectron-hole. Fig. 6e shows the fluorescence of Fe-g-C_3N_4 before and after the introduction of H_2O_2. The photocatalysis-Fenton system fluorescence peak was reduced by 24% versus the Fe-g-C_3N_4 fluorescence peak. This shows that the addition of H_2O_2 can further inhibit the recombination of photo-generated electrons and holes. Through photocurrent, impedance and fluorescence detection, we showed that the

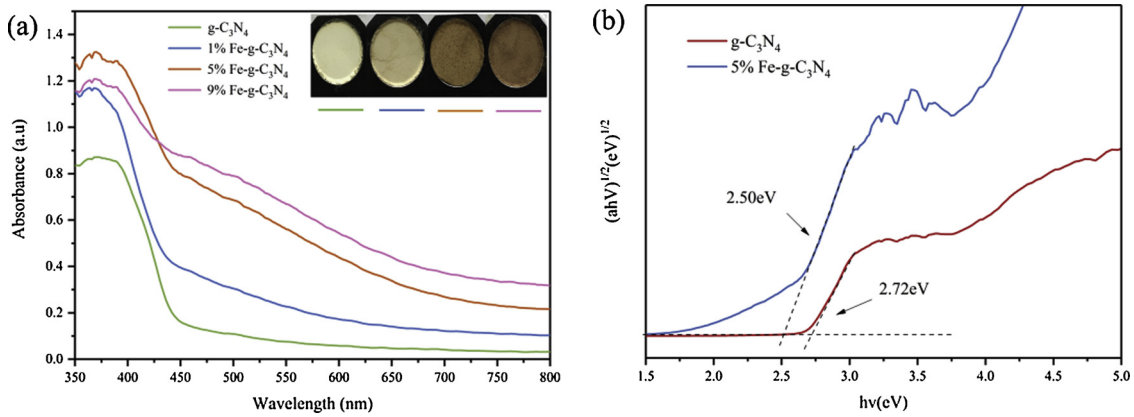

Fig. 5. UV–vis diffuse reflectance spectra of g-C_3N_4 and Fe-g-C_3N_4, (b) The Kubelka-Munk function curve of g-C_3N_4 and Fe-g-C_3N_4.

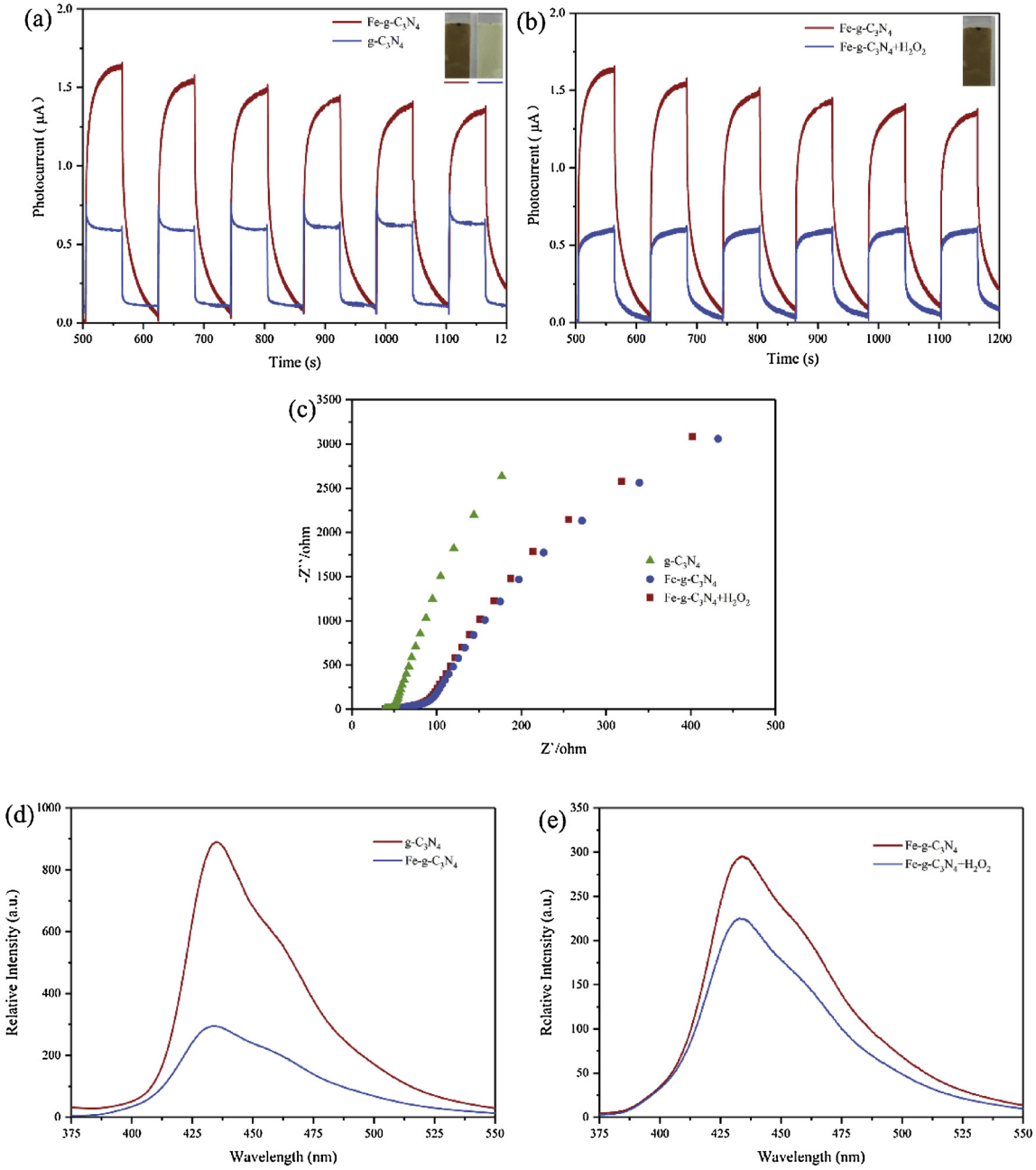

Fig. 6. (a) Transient photocurrent responses of g-C_3N_4 and Fe-g-C_3N_4, (b) Transient photocurrent responses of g-C_3N_4 adding H_2O_2, (c) EIS plots and bode-phase plots of g-C_3N_4 and Fe-g-C_3N_4, (d) PL spectra of g-C_3N_4 and Fe-g-C_3N_4, (e) PL spectra of Fe-g-C_3N_4 with adding H_2O_2. (Potentials: 0.5 V, electrolyte: 0.1 M Na_2SO_4, H_2O_2 = 8 mM, P = 350 W Xenon lamp > 420).

photo-electron transfer to Fe rapidly inhibits the recombination of electron-hole and photo-electrons are consumed in the Fenton reaction and participate in the Fenton reaction.

Trapping experiments and ˙OH detection experiments were performed to further study the mechanism of the photocatalysis-Fenton system. In Fig. 7a, we note that without the addition of trapping agents, the removal efficiency by Fe-g-C_3N_4 reaches 90.4% at 1 h. The removal efficiency was significantly reduced after adding isopropanol to the reaction system. This actual value was only 17.6% (a reduction of 72.9%). The removal efficiency also slightly decreased after adding Cr (VI). This actual value was 65.5% (a reduction of 24.9%). The removal efficiency was slightly reduced after the addition of p-benzoquinone—the removal efficiency was 73.2% and it decreased by 17.2%. The removal efficiency was almost unchanged after the addition of EDTA-2Na. This phenomenon may indicate that ˙OH is the main active species and $\cdot O^{2-}$ and e- are the secondary active species.

To further verify that ˙OH is the main species of the reaction, ˙OH generation was monitored. Fig. 7b shows the fluorescence spectra of photocatalytic reaction, Fenton reaction and photocatalysis-Fenton system for 20 min. There is very little fluorescence at 420 nm in the photocatalytic reaction, but the Fenton reaction produces a strong fluorescence peak. The photocatalysis-Fenton system fluorescence intensity increased by 47.4% compared to Fenton reaction. This further proves that the photocatalysis-Fenton system of active species is ˙OH and the photocatalysis-Fenton system can accelerate the Fenton reaction and the photocatalytic reaction to produce ˙OH, which is consistent with the activity of phenol removal in Fig. 1a. To further study the mechanism of photocatalysis-Fenton system, Fig. 7c shows the detection of ˙OH intensities before and after adding Cr (VI). The intensity of the fluorescence peak was reduced by 73.6% after adding Cr (VI)

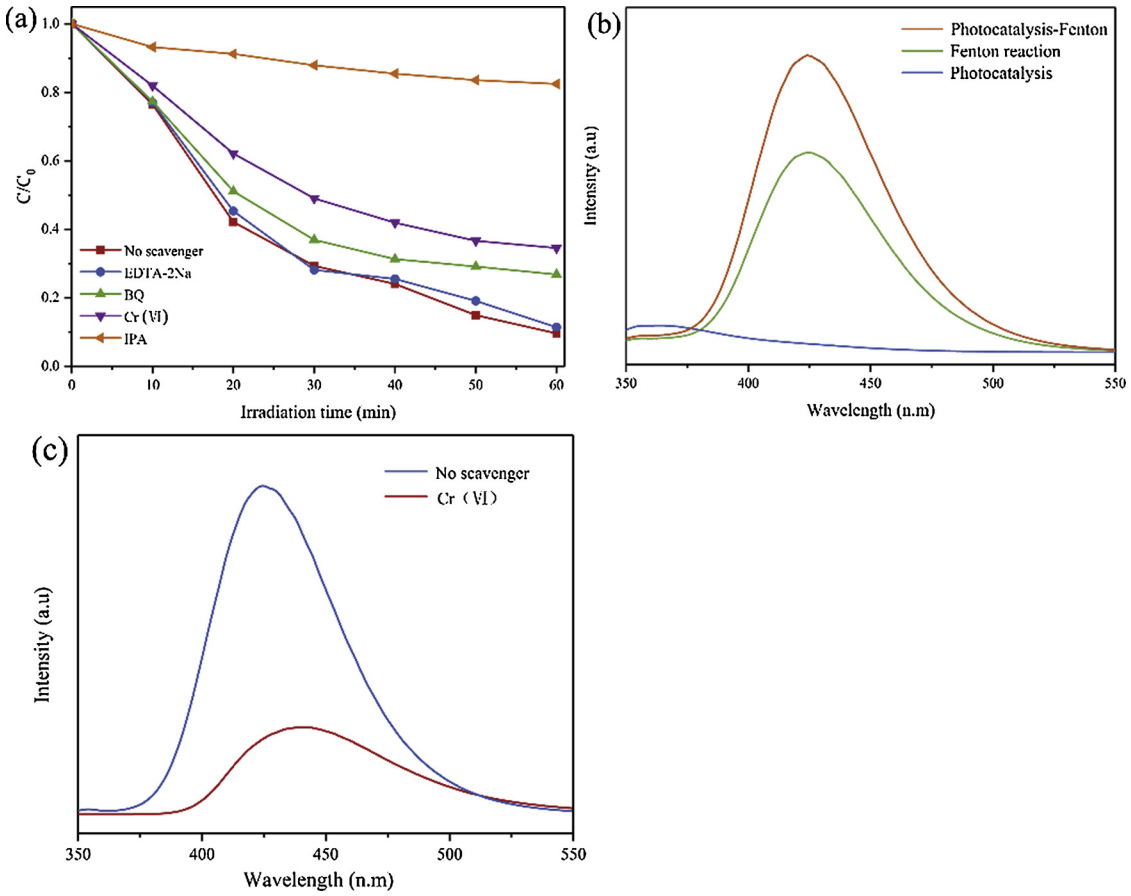

Fig. 7. (a) Change of phenol removal degree observed for photocatalysis-Fenton system under visible light irradiation in the presence of various trapping agents, (b) Concentration of ˙OH generated at photocatalysis, Fenton reaction and photocatalysis-Fenton system in 20 min, (c) Concentration of ˙OH generated at photocatalysis-Fenton system with Cr(VI).

indicating that the ˙OH content was significantly reduced and e^- was an important factor in the production of ˙OH. This further proved that the electrons were transferred to Fe and participated in the Fenton reaction, which assisted in the conversion of Fe^{3+} to Fe^{2+} and increased the amount of ˙OH. This result is consistent with the above photocurrent test results. The valence band structure of the catalyst was analyzed in Fig. S2. It can be found that the valence bands of g-C_3N_4 and Fe-g-C_3N_4 catalysts are 1.40 eV, indicating that Fe doping of g-C_3N_4 did not affect the valence band position of g-C_3N_4.

Based on the above trapping experiments, an ˙OH detection and e^- transfer mechanism for the photocatalysis-Fenton system removal phenol was proposed. Scheme 3 shows that the Fe-g-C_3N_4 nanoparticles generate electrons and holes under visible irradiation. Some of the photo-generated electrons react with O_2 in the reaction solution to produce $\cdot O^{2-}$, which oxidizes phenol to produce CO_2 and H_2O. The other part of the photo-electron can be quickly transferred to the Fe^{3+} in the catalyst to form Fe^{2+}. Subsequently, the generated Fe^{2+} ions react with H_2O_2 to produce ˙OH radicals that can oxidize phenol. After a series of reactions, phenol eventually produces CO_2 and H_2O. The H_2O_2 in the system also reacts with holes to form O_2 and H^+, which in turn can provide more O_2 for the formation of $\cdot O^{2-}$.The traditional homogeneous or heterogeneous Fenton systems usually generate ˙OH radicals catalytically via oxidation of Fe^{2+} to Fe^{3+} followed by reduction back to Fe^{2+} by another molecule of H_2O_2. In contrast, the photocatalysis-Fenton system can excite electrons to assist in the conversion of Fe^{3+} to Fe^{2+}. Thus, the consumption of H_2O_2 can be reduced to some extent.

Fig. S1 shows a representative mass spectrum of the phenol degradation process. Fragment molecules such as catechol, benzene-1, 2, 3-triol, (Z)-2-hydroxyhex-3-enedioic acid, (Z)-hex-3-enedioic acid, oxalic acid were found. Therefore, the mechanism of phenol degradation is inferred as follows Scheme S1. Firstly, ˙OH attacks the ortho or para position of phenol to form catechol and benzene-1, 2, 3-triol. Secondly, this compound was further undergo ring break and form (Z)-2-hydroxyhex-3-enedioic acid, that will degrade to (Z)-hex-3-enedioic acid. Finally, the mineralization will take place to H_2O and CO_2. Similar trend of the products was also observed by recent reports [56–58].

3.3. Photocatalysis-Fenton system condition optimization

Fig. S3a shows the effect of different Fe doping amounts of Fe-g-C_3N_4 to the phenol removal efficiency in 50 min. The Fe doping amount was 1% to 5%, removal efficiency increases from 40.0% to 100%. The Fe doping amount increases to 9%, the removal efficiency is reduced to 72%. The Fe doping reaches 5% exhibits the best removal ability. This is because when the Fe doping amount is small, the photocatalysis-Fenton system process involves a small amount of circulating Fe, a small amount of ˙OH generated by the H_2O_2. However, if the Fe content is too high, can be explained by the fact that excess Fe species may act as recombination centers for photo-induced electrons and holes and/or cover the active sites on the g-C_3N_4 surface and thereby reduce the efficiency of charge separation. Electronic cannot participate in Fenton reaction effectively [47]. Therefore, the photocatalysis-Fenton system equilibrium is achieved when Fe doping reaches 5% and the electrons generated by Fe-g-C_3N_4 effectively promote the Fe ion cycle in the Fenton reaction.

Fig. S3b shows the effect of different H_2O_2 concentrations on the efficiency of photocatalysis-Fenton system phenol removal. The 50 min removal efficiency increased from 20.2% to 100% when the initial

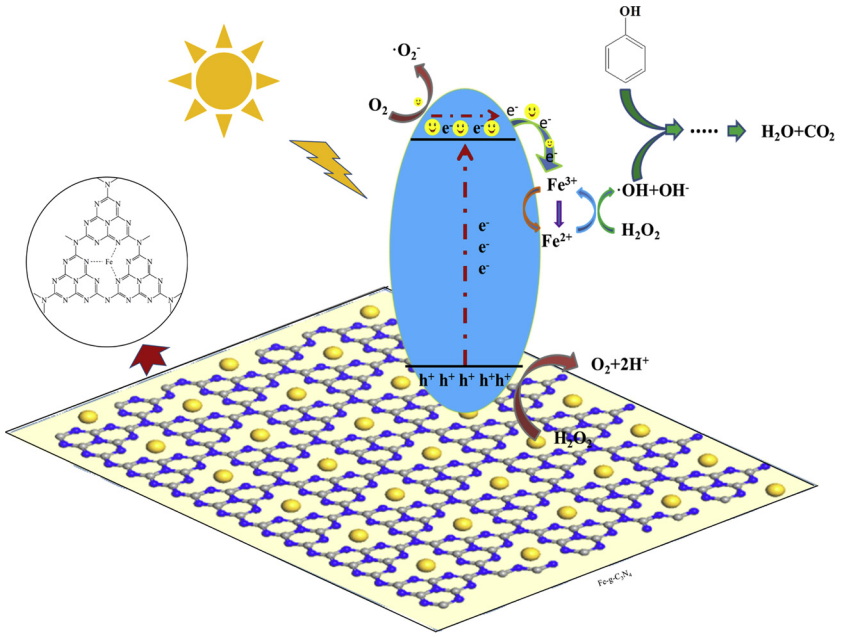

Scheme 3. The plausible mechanism of the photocatalysis-Fenton system with Fe-g-C_3N_4.

H_2O_2 concentration of the phenol solution increased from 2 mM to 8 mM—an improvement of 3.9 fold. However, when the concentration of H_2O_2 was further increased to 10 mM, the removal efficiency was 97.4% and the removal efficiency was slightly decreased. This result is attributed to the increase in the concentration of H_2O_2 that can provide more ˙OH for the catalytic reaction. However, if the H_2O_2 concentration is too high, then excess H_2O_2 will react with ˙OH (˙OH + H_2O_2 → ˙HO_2 + H_2O) resulting in catalytic ·HO_2 that reacts with ˙OH to generate O_2 and H_2O (HO_2 + ˙OH → O_2 + H_2O) [24]. A large amount of ˙OH is consumed and ˙OH does not react with phenol efficiently resulting in a reduction in the removal efficiency and wasted H_2O_2.

Fig. S3c shows the efficiency of the photocatalysis-Fenton system for removing phenol at different pH values (The pH was adjusted by 0.1 M sulfuric acid and 0.1 M sodium hydroxide). At 20 min, the photocatalysis-Fenton system removal efficiency at pH = 11, 7 and 3 was 9.8%, 44.7% and 84.3%, respectively. The photocatalysis-Fenton system has best removal efficiency under acidic conditions perhaps because Fe doped into g-C_3N_4 produces different ligands at different pH values. When the pH was 3, the ligands increased the removal efficiency and water was replaced by OH^- on the surface of the catalyst under alkaline conditions—this is not conducive to H_2O_2 production ˙OH [59]. H_2O_2 can be rapidly decomposed into H_2O and O_2 under alkaline conditions to accelerate the consumption of H_2O_2.

Fig. S3d compares the photocatalysis-Fenton system removal efficiency of phenol with different catalyst concentrations at 20 min (0.2, 0.5, 1.0, 1.5, 2.0 and 2.5 g/L). When the catalyst concentration increased from 0.2 g/L to 1.5 g/L, the efficiency increased from 28.8% to 98.2%—this was a 2.4 fold increase. However, the catalyst concentration to 2.5 g/L, the removal efficiency was 97.0%, which means that the removal efficiency was slightly reduced. This is because when the amount of catalyst is gradually increased, more electrons can be generated due to the increase in the catalyst; thus, a large amount of Fe participates in the Fenton reaction cycle so that H_2O_2 conversion to ˙OH is accelerated. However, if there are too many catalysts, then the absorption of light by the catalyst is affected. Light cannot be completely irradiated and the excitation of electrons is severely affected; thus, the production of ˙OH is reduced and the activity tends to decrease. On the other hand, too much catalyst will generate excess Fe^{2+} and Fe^{2+} will also react with OH in the system and consume ˙OH (OH + Fe^{2+} → Fe^{3+} + OH^-) [60]; thus, the efficiency of phenol removal is slightly reduced.

Fig. 8a shows the removal efficiency of phenol for photocatalysis-Fenton system over five cycles. After five cycles, the removal efficiency was 98.0%, 95.2%, 93.4%, 91.0% and 88.0%, respectively and it then was reduced by 10.0%. It is speculated that this may be due to that the catalyst be lost which is rarely dissolved in the phenol solution during the cycle. The concentration of Fe ion in the solution after each cycle was 0.147, 0.011, 0.005, 0.010 and 0.003 ppm, respectively. After the first cycle, the Fe ion leaching efficiency was only 0.35% and the ion leaching efficiency then approached zero. This shows that almost all of the Fe was successfully incorporated into the g-C_3N_4 skeleton and only a small amount of unincorporated Fe was thawed into the reaction solution in the first cycle. As the number of cycle's increases, the ion leaching efficiency is almost zero further illustrating that Fe ions are effectively immobilized on g-C_3N_4 under the action of chemical bonding. Versus the traditional homogeneous Fenton reaction, the heterogeneous photocatalysis-Fenton system not only accelerates the removal efficiency of pollutants, but also reduces the cost of catalysts and has large-scale application value.

The phenol, bisphenol A and 2, 4-dichlorophenol removal experiments were conducted to further explore the photocatalysis-Fenton system for the removal ability of other pollutants. The removal efficiency at 20 min was evaluated with OPC, COD and TOC (Fig. 8b). The concentration of phenol, bisphenol A and 2, 4-dichlorophenol was reduced by 62.8%, 70.0% and 74.6%. The decrease in the COD and TOC values in the water indicates that the pollutants were mineralized to CO_2 and H_2O. Here, the COD removal efficiency s of phenol, bisphenol A and 2,4-dichlorophenol were 47.9%, 65.9% and 69.0%, respectively and the TOC removal efficiency s were 35.7%, 46.0% and 49.0%, respectively. This shows that the photocatalysis-Fenton system has high efficiency removal ability for different pollutants and realizes the mineralization of pollutants. The change in the HPLC peak 2D pattern of organic matter in Fig. 1c also illustrates this problem. Different pollutants show different removal efficiencies in the Fig. 8b, the possible reason are described as follow. The degradation rates of phenol, bisphenol A and 2, 4-dichlorophenol at 20 ppm by Photocatalysis-Fenton system degradation of Fe-g-C_3N_4 were 62.8%, 70.0% and 74.6%, respectively. In the case of the same degradation reaction conditions, the nuances of the degradation rate should be caused by the different structures of the three organic pollutants. The ionization equilibrium

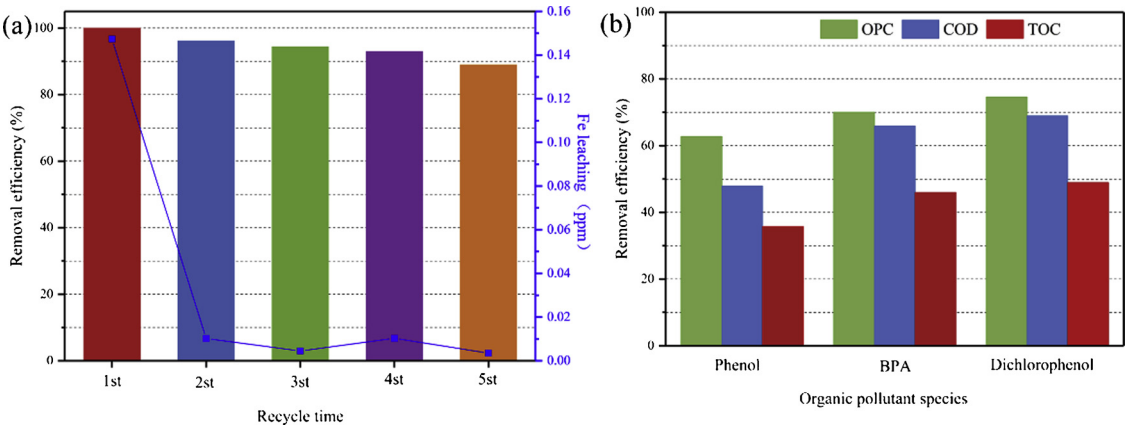

Fig. 8. (a) Comparing the removal efficiency of photocatalysis-Fenton system to different contaminants, (b) Cycling removal of phenol for photocatalysis-Fenton system under visible irradiation. (C_0 = 20 ppm, H_2O_2 = 8.00 mM, catalyst = 1.0 g/L, pH = 3, P = 350 W Xenon lamp > 420, T = 25 ± 2 °C).

exists in the solution of phenol, bisphenol A and 2, 4-dichlorophenol. The equilibrium equation is shown in Scheme S2. After ionization, a negatively charged phenoxy anion or substituted phenoxy anion is formed, which is adsorbed on the surface of the catalyst by electrostatic interaction with a catalyst having a positive charge on the surface (the zeta potential of the Fe-g-C_3N_4 catalyst is +32.2). The pKa values of phenol, bisphenol A and 2, 4-dichlorophenol are 9.98, 9.59 and 8.09, respectively. The smaller the pKa of the pollutants, the more negative ions will be present in the solution. And the pollutants adsorbed on the catalyst surface by electrostatic interaction. The more the pollutants adsorbed on the surface of the catalyst react directly with active species such as holes and hydroxyl groups, so the degradation rate is higher under the same conditions. This is consistent with the trend of degradation of phenol, bisphenol A and 2, 4-dichlorophenol. The adsorption of three pollutants on the catalyst surface is shown in Table S1. The adsorption rate of the catalyst surface was measured at a concentration of 5 ppm for 30 min. The adsorption capacity of phenol, bisphenol A and 2, 4-dichlorophenol increased gradually, which was consistent with the trend of the degradation rate data of the three. Among the degradation activities of Fe-g-C_3N_4 on phenol, bisphenol A and 2, 4-dichlorophenol, the adsorption amount of the three on the catalyst surface is very small, indicating that adsorption is not the main factor of the degradation process. This difference in adsorption results in subtle differences in the rate of degradation when other degradation conditions are the same [61,62]

3.4. Photocatalysis-Fenton system removal of complex wastewater

By simulating pollutants with phenol, the photocatalysis-Fenton system mechanism was explored and the relevant conditions were optimized. The optimum active conditions were explored: the doping amount of the catalyst Fe-g-C_3N_4 was 5%, the concentration of H_2O_2 is maintained at 8 mM, the pH is approximately 3 and the concentration of the catalyst is 1.5 g/L. Based on the above research results, the system was extended to a complex wastewater system. Coking wastewater is a very serious problem because it contains strong toxic phenolic compounds, polycyclic aromatic hydrocarbons compounds. Fig. S4 shows the removal efficiency of 50 ml coking wastewater in 60 min when the amount of catalyst and H_2O_2 is increased by different multiples under simulated sunlight. The catalyst and H_2O_2 usage increased from a (a: catalyst = 1.5 g/L, H_2O_2 = 8.0 mM) to c (c: catalyst = 3.0 g/L H_2O_2 = 16.0 mM) and the removal efficiency of COD and TOC increased from 29.4% and 20.3% to 82.4% and 67.8% respectively. However, when the dosage of catalyst and H_2O_2 was increased (d: catalyst = 3.8 g/L, H_2O_2 = 20.0 mM), the COD and TOC removal efficiency decreased to 70.6% and 59.1%. When the dosage of catalyst is 3.0 g/L and the concentration of H_2O_2 is 16 mM, the coking wastewater exhibits excellent removal capacity. The COD and TOC values are from 64.6 and 25.3 mg/L reduced to 11.4 and 8.1 mg/L, respectively; thus, the coking wastewater discharge standards are achieved.

The feasibility of photocatalysis-Fenton system removal of coking wastewater was further analyzed with 300 ml coking wastewater. Photocatalytic (Fe-g-C_3N_4 + light), homogeneous Fenton reaction ($FeSO_4$ + H_2O_2) and photocatalysis-Fenton system (Fe-g-C_3N_4 +light

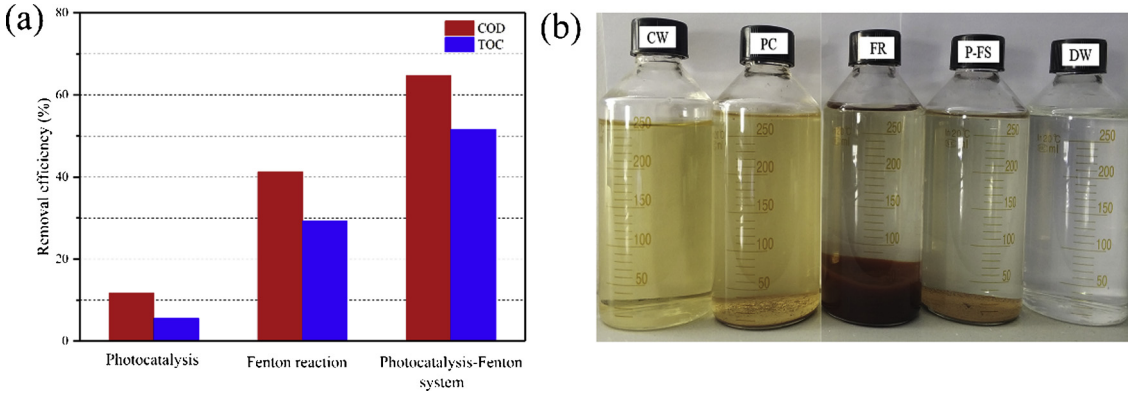

Fig. 9. (a) Effect of Photocatalysis, Fenton reaction and photocatalysis-Fenton system on removal efficiency of 300 ml of coking wastewater, (b) The 300 ml coking wastewater after reaction under different conditions. (Coking wastewater = 300 ml, Catalyst = 3.0 g/L, H_2O_2 = 16.00 mM, pH = 3, P = 500 W Xenon lamp, CW: coking wastewater, PC: photocatalysis, FR: Fenton reaction, P-FS: photocatalysis-Fenton system, DW: distilled water).

+ H_2O_2) were used to treat coking wastewater under the same conditions. After 60 min, photocatalytic, homogeneous Fenton reaction and photocatalysis-Fenton system COD values were 57.0, 38.0 and 22.8 mg/L, respectively and the removal efficiency were 11.7%, 41.1% and 64.71% (Fig. 9a). The TOC values were 23.9 L, 17.8 and 12.2 mg/L, respectively and the removal efficiency were 5.5%, 29.3% and 51.6%, respectively. The photocatalysis-Fenton system removal efficiency of COD and TOC was 57.1% and 76.1% higher than traditional Fenton reaction, respectively.

Fig. 9b is a physical map of coking wastewater removal. From left to right, the color of the coking wastewater gradually clarifies, which shows that the photocatalysis-Fenton system decolorizes the sample. After 60 min of reaction, the coking wastewater turns from orange to colorless. The homogeneous Fenton reaction produces a large amount of $Fe(OH)_3$ reddish brown sludge after the reaction is terminated. This can cause secondary pollution in industrial production. Heterogeneous photocatalysis-Fenton system consists of in-situ doped Fe-g-C_3N_4 catalyst that can not only improve the removal efficiency, but can also precipitate the catalyst to the bottom. This is easy to recycle and reuse and minimizes catalyst cost.

The photocatalysis-Fenton system has better economic benefits than the homogeneous Fenton reaction. Fig. S5 shows COD and TOC removal efficiency of different H_2O_2 concentrations. Fig. S5a shows that the COD removal efficiency s at 16 mM H_2O_2 was 45.0%. The COD removal efficiency increased to 74.6% at 32 mM H_2O_2. The COD removal efficiency gradually increases with increasing H_2O_2 concentration. Fig. S5b shows similar trends as in Fig. S5a. The TOC removal efficiency was 26.3% at 16 mM H_2O_2. The TOC removal efficiency increased to 54.5% at 32 mM H_2O_2. The removal efficiency was basically the same for the Fenton reaction with 32 mM H_2O_2 and the photocatalysis-Fenton system H_2O_2 concentration of 16 mM. The same removal capacity is achieved, but the photocatalysis-Fenton system saves about half of H_2O_2compared to homogeneous Fenton reactions.

Fig. S6 compares the COD and TOC removal efficiency of homogeneous Fenton reactions at different times. Fig. S6a shows that the COD removal efficiency of the 60 min was 45.0%. After 120 min, the COD removal efficiency increased to 69.4%. The COD removal efficiency gradually increases with increasing reaction time. Fig. S6b shows similar trends to Fig. S6a. The TOC removal efficiency at 60 min was 26.3%. After 120 min, the TOC removal efficiency increased to 54.5%. The Fenton reaction at 120 min and photocatalysis-Fenton system at 60 min removal efficiency were basically the same as the control. The same removal capacity is achieved; photocatalysis-Fenton system saves nearly half the reaction time compared to homogeneous Fenton reactions.

In the additional literature Table S2, we have listed some recent reports on the degradation of organic pollutants by photocatalysis and photocatalysis-Fenton systems. It can be found that the use of g-C_3N_4 as a photocatalyst has very low catalytic performance in removing phenol, MB, RhB, amido black 10B and other contaminants, such as: g-C_3N_4@ppy-rGO photocatalyst degrades 10 ppm of phenol under visible light for 550 min. The removal efficiency is 80% [63]. As a photocatalytic-Fenton system, the catalytic activity is greatly improved. For example, the degradation efficiency of 30 mg/L MB using g-C_3N_4/MOF catalyst is 100% in 120 min [64]. The Fe-g-C_3N_4 photocatalytic-Fenton system catalyst studied in this paper has high catalytic efficiency. After 50 min, the phenol removal rate can reach 100%, and after optimization, the actual wastewater (coking wastewater) is also expressed. With excellent removal effect, the COD value of coking wastewater can be reduced from 64.6 mg/L to 22.8 mg/L after 60 minutes, reaching the national emission standard. This study provides a new idea for environmental restoration issues.

4. Conclusions

An in situ Fe-doped Fe-g-C_3N_4 catalyst was successfully synthesized by a simple method. The Fe^{3+} with N in ri-s-triazine (heptazine) structures forms an σ-π coordinate bond and this makes Fe^{3+} firmly fixed to the g-C_3N_4 skeleton. The H_2O_2 was added to form a photocatalysis-Fenton system and it shows excellent phenol removal ability under visible irradiation. The photocatalysis-Fenton system removed 20 ppm phenol in 50 min. The reaction efficiency is 59.9% higher than the Fenton reaction alone in 50 min. The introduction of Fe in g-C_3N_4 catalyst can accelerate the separation of photoelectron-holes and can rapidly transfer electrons to Fe. The Fe accepts photoelectrons to realize rapid reduction from trivalent to divalent, which in turn promotes the rapid generation of strong oxidative $^{\cdot}OH$ in H_2O_2. Therefore, photocatalytic and Fenton reactions were synergistically enhanced to remove organic pollutants. The best active conditions for removal of phenol were explored: the doping amount of catalyst Fe-g-C_3N_4 was 5%, the concentration of H_2O_2 in the reaction system was 8 mM, the pH was 3 and the catalyst dosage was 1.5 g/L. The system also exhibits excellent removal of complex wastewater such as coking wastewater. Compared with the homogeneous Fenton reaction, the photocatalysis-Fenton system COD and TOC removal capacities of coking wastewater increased by 57.2% and 76.1%, respectively. The same removal capacity is achieved; the photocatalysis-Fenton system saves about half of the required H_2O_2 and reaction time versus the homogeneous Fenton reaction. The photocatalysis-Fenton system treats complex wastewater has a very broad prospect. This offers a new idea for current environmental pollution control.

Acknowledgements

This work was financially supported by the National Natural Science Foundation of China (No. 51672081), the support program for one hundred excellent talents of innovation in Hebei provincial universities (III) (No. SLRC2017049), Youth Fund Project of Hebei Province Department of Education (QN2018056), Science and Technology Research Project for Tangshan City (18130213A).

Appendix A. Supplementary data

Supplementary material related to this article can be found, in the online version, at doi:https://doi.org/10.1016/j.apcatb.2018.12.029.

References

[1] H. Ramezanalizadeh, F. Manteghi, J. Clean Prod. 172 (2018) 2655–2666.
[2] H. Wang, Y. Liang, L. Liu, J. Hu, P. Wu, W. Cui, Appl. Catal. B: Environ. 208 (2017) 22–34.
[3] Y. Liang, S. Lin, L. Liu, J. Hu, W. Cui, Appl. Catal. B: Environ. 164 (2015) 192–203.
[4] W. Cui, W. An, L. Liu, J. Hu, Y. Liang, J. Hazard. Mater. 280 (2014) 417–427.
[5] H. Wang, Y. Wu, M. Feng, W. Tu, T. Xiao, T. Xiong, H. Ang, X. Yuan, J. Chew, Water Res. 144 (2018) 215–225.
[6] Y. Pi, X. Li, Q. Xia, J. Wu, Y. Li, J. Xiao, Z. Li, Chem. Eng. J. 337 (2018) 351–371.
[7] Y. Li, W. Cui, L. Liu, R. Zong, W. Yao, Y. Liang, Y. Zhu, Appl. Catal. B: Environ. 199 (2016) 412–423.
[8] R. Berenguer, J. Sieben, C. Quijada, E. Morallón, Appl. Catal. B: Environ. 199 (2016) 394–404.
[9] M. Ateia, M. Ceccato, A. Budi, E. Ataman, C. Yoshimura, M. Johnson, Chem. Eng. J. 335 (2018) 384–391.
[10] F. Chen, W. An, L. Liu, Y. Liang, W. Cui, Appl. Catal. B: Environ. 217 (2017) 65–80.
[11] J. Pignatello, E. Oliveros, A. MacKay, Crit. Rev. Environ. Sci. Technol. 36. 1 (2006) 1–84.
[12] Y. Zhang, W. Cui, W. An, L. Liu, Y. Liang, Y. Zhu, Appl. Catal. B: Environ. 221 (2018) 36–46.
[13] L. Zhou, L. Wang, J. Zhang, J. Lei, Y. Liu, Eur. J. Inorg. Chem. 2016 (2016) 5387–5392.
[14] Y. Wu, H. Wanga, W. Tu, Y. Liu, S. Wu, Y. Tan, Jia W. Chew, Appl. Catal. B: Environ. 233 (2018) 58–69.
[15] D. Chatterjee, S. Dasgupta, J. Photochem. Photobiol. C 6 (2005) 186–205.
[16] L. Sun, T. Du, C. Hu, J. Chen, J. Lu, Z. Lu, H. Han, ACS Sustain. Chem. Eng. 5 (2017) 8693–8701.
[17] Y. Choi, H. Jung, W. Shin, Y. Sohn, Appl. Surf. Sci. 356 (2015) 615–625.
[18] K. Nakata, A. Fujishima, J. Photochem. Photobiol. C 13 (2012) 169–189.
[19] Y. Wang, W. Yang, X. Chen, J. Wang, Y. Zhu, Appl. Catal. B: Environ. 220 (2018) 337–347.
[20] S. Thangavel, K. Krishnamoorthy, V. Krishnaswamy, N. Raju, S.J. Kim,

G. Venugopal, J. Phys. Chem. C 119 (2015) 22057–22065.
[21] X. Nguyen, G. Zhang, X. Yang, ACS Appl. Mater. Interfaces 9 (2017) 8900–8909.
[22] S. Guo, G. Zhang, J. Yu, J. Colloid. Interf. Sci. 448 (2015) 460–466.
[23] C. Xiao, J. Li, Ga. Zhang, J. Clean. Prod. 180 (2018) 550–559.
[24] C. Cai, Z. Zhang, J. Liu, N. Shan, H. Zhang, D. Dionysiou, Appl. Catal. B: Environ. 182 (2016) 456–468.
[25] Q. Sun, Y. Hong, Q. Liu, L. Dong, Appl. Surf. Sci. 430 (2018) 399–406.
[26] X. Wang, Y. Liang, W. An, J. Hu, Y. Zhu, W. Cui, Appl. Catal. B: Environ. 219 (2017) 53–62.
[27] M. Wen, T. Xiong, Z. Zang, W. Wei, X. Tang, Dong Opt. Express 24 (2016) 10205–10212.
[28] Y. Wu, H. Wang, W. Tu, S. Wu, Y. Liu, Y. Tan, H. Luo, X. Yuan, J. Chew, Appl. Catal. B: Environ. 229 (2018) 181–191.
[29] Y. Wu, H. Wang, Y. Sun, T. Xiao, W. Tu, X. Yuan, G. Zeng, S. Li, J. Chew, Appl. Catal. B: Environ. 227 (2018) 530–540.
[30] Y. Wang, Y. Di, M. Antonietti, H. Li, X. Chen, X. Wang, Chem. Mater. 22 (2010) 5119–5121.
[31] X. Song, H. Tao, L. Chen, Y. Sun, Mater. Lett. 116 (2014) 265–267.
[32] S. Hu, R. Jin, G. Lu, D. Liu, J. Gui, RSC Adv. 4 (2014) 24863–24869.
[33] J. Ma, Q. Yang, Y. Wen, W. Liu, Appl. Catal. B: Environ. 201 (2017) 232–240.
[34] H. Wang, Y. Liang, L. Liu, J. Hu, W. Cui, J. Hazard. Mater. 344 (2018) 369–380.
[35] L. Zhang, K. Wong, H. Yip, C. Hu, J. Yu, P. Wong, Environ. Sci. Technol. 44. 4 (2010) 1392–1398.
[36] K. Wang, H. Niu, J. Chen, J. Song, C. Mao, S. Zhang, Y. Gao, Appl. Surf. Sci. 404 (2017) 138–145.
[37] C. Liang, Y. Liu, K. Li, J. Wen, S. Xing, Z. Ma, Y. Wu, Sep. Purif. Technol. 188 (2017) 105–111.
[38] X. Wang, W. Yang, F. Li, Y. Xue, R. Liu, Y. Hao, Ind. Eng. Chem. Res. 52 (2013) 17140–17150.
[39] Z. Wei, F. Liang, Y. Liu, W. Luo, J. Wang, W. Yao, Y. Zhu, Appl. Catal. B: Environ. 201 (2017) 600–606.
[40] Q. Liu, Y. Guo, Z. Chen, Z. Zhang, X. Fang, Appl. Catal. B: Environ. 183 (2016) 231–241.
[41] X. Du, J. Wan, J. Jia, C. Pan, X. Hu, J. Fan, E. Liu, Mater. Design. 119 (2017) 113–123.
[42] K. Lv, X. Guo, X. Wu, Q. Li, W. Ho, M. Li, H. Ye, D. Du, Appl. Catal. B: Environ. 199 (2016) 405–411.
[43] B. Li, X. Chen, T. Zhang, S. Jiang, G. Zhang, W. Wu, X. Ma, Appl. Surf. Sci. 439 (2018) 1047–1056.
[44] Y. Tan, Z. Shu, J. Zhou, T. Li, W. Wang, Z. Zhao, Appl. Catal. B: Environ. 230 (2018) 260–268.
[45] Y. Xu, L. Zhang, M. Yin, D. Xie, J. Chen, J. Yin, Y. Fu, P. Zhao, H. Zhong, Y. Zhao, X. Wang, Appl. Surf. Sci. 440 (2018) 170–176.
[46] F. Li, Z. Yu, H. Shi, Q. Yang, Q. Chen, Y. Pan, G. Zeng, L. Yan, Chem. Eng. J. 322 (2017) 33–45.
[47] S. Tonda, S. Kumar, S. Kandula, V. Shanker, J. Mater. Chem. A 2. 19 (2014) 6772–6780.
[48] Q. Liu, T. Chen, Y. Guo, Z. Zhang, X. Fang, Appl. Catal. B: Environ. 205 (2017) 173–181.
[49] L. Shi, W. Ding, S. Yang, Z. He, S. Liu, J. Hazard. Mater. 347 (2018) 431–441.
[50] L. Shi, S. Liu, Z. He, Appl. Surf. Sci. 457 (2018) 1035–1043.
[51] X. Xie, Y. Liu, X. Dong, C. Lin, X. Wen, Q. Yan, Appl. Surf. Sci. 455 (2018) 742–747.
[52] F. Dong, Z. Zhao, T. Xiong, Z. Ni, W. Zhang, Y. Sun, W.K. Ho, ACS Appl. Mater. Inter. 5 (2013) 11392–11401.
[53] L. Liu, Y. Qi, J. Lu, S. Lin, W. An, Y. Liang, W. Cui, Appl. Catal. B: Environ. 183 (2016) 133–141.
[54] S.C. Yan, Z.S. Li, Z.G. Zou, Langmuir. 25 (2009) 10397–10401.
[55] S. Hu, R. Jin, G. Lu, D. Liu, J. Gui, Rsc Adv. 4. 47 (2014) 24863–24869.
[56] M. Rani, U. Shanker, Colloid. Surf. A 553 (2018) 546–561.
[57] M. Rani, U. Shanker, Environ. Nanotechnol., Monit. Manage. 10 (2018) 36–50.
[58] M. Rani, U. Shanker, J. Environ. Chem. Eng. 6. 1 (2018) 1512–1521.
[59] J. Zhang, J. Zhuang, L. Gao, Y. Zhang, N. Gu, J. Feng, D. Yang, J. Zhu, X. Yan, Chemosphere 73 (2008) 1524–1528.
[60] M. Umar, H.A. Aziz, M.S. Yusoff, Waste Manage. 30 (2010) 2113–2121.
[61] L. Liu, M. Yue, J. Lu, J. Hu, Y. Liang, W. Cui, Appl. Surf. Sci. 456 (2018) 645–656.
[62] W. Cui, J. He, H. Wang, J. Hu, L. Liu, Y. Liang, Appl. Catal. B: Environ. 232 (2018) 232–245.
[63] Yi. Liang, X. Wang, W. An, Y. Li, J. Hu, W. Cui, Appl. Surf. Sci. 466 (2019) 666–672.
[64] X. Li, Y. Pi, L. Wu, Q. Xia, J. Wu, Z. Li, J. Xiao, Appl. Catal. B: Environ. 202 (2017) 653–663.